

## Surface-to-tunnel seismic tomography studies at Yucca Mountain, Nevada

Roland Gritto, Valeri A. Korneev, and Thomas M. Daley

Center for Computational Seismology, Earth Sciences Division, Lawrence Berkeley National Laboratory, Berkeley, California, USA

Mark A. Feighner

Department of Mathematics and Sciences, Solano Community College, Fairfield, California, USA

Ernest L. Majer and John E. Peterson

Center for Computational Seismology, Earth Sciences Division, Lawrence Berkeley National Laboratory, Berkeley, California, USA

Received 17 June 2002; revised 1 November 2003; accepted 17 December 2003; published 27 March 2004.

[1] A surface-to-tunnel seismic survey was conducted to estimate fracture intensity and distribution in the proposed nuclear waste repository area at Yucca Mountain, Nevada. A 5-km-long source line and a 3-km-long receiver line were located on top of Yucca Mountain ridge and inside the Exploratory Study Facility (ESF) tunnel, respectively. Numerical modeling showed that the first arrival *P* waves are mainly propagated in the repository horizon at depth. Therefore two-dimensional travel time inversions were performed after the actual source locations on the ridge were projected onto the layer of interest at depth. Static corrections were applied to absorb the scatter in the new source locations and to correct for variations in source and receiver coupling and travel time shifts. Zero-offset amplitude variations of the first arrivals across the receiver line inside the tunnel showed strong correlation with the fracture density determined by measurements along the tunnel wall. Wave guidance by subhorizontal fractures is suggested as a possible source for this phenomenon. Tomographic inversion of the travel time data revealed a low-velocity zone in the south central area of the repository horizon. Conversion of the velocity tomography results to fracture-density tomograms showed good correlation with fracture intensity mapped along tunnel walls. The fractured zone extends over a large area in the southern region of the potential repository, in particular, southwest of the intensely fractured zone encountered in the ESF tunnel. The rock in the northern section of the repository appears more competent compared to the highly fractured areas in the south. **INDEX TERMS:** 0935 Exploration Geophysics: Seismic methods (3025); 7203 Seismology: Body wave propagation; 8180 Tectonophysics: Tomography; **KEYWORDS:** wave propagation in fractured tuff, surface-to-tunnel tomographic imaging, FD modeling, velocity and fracture density estimation

**Citation:** Gritto, R., V. A. Korneev, T. M. Daley, M. A. Feighner, E. L. Majer, and J. E. Peterson (2004), Surface-to-tunnel seismic tomography studies at Yucca Mountain, Nevada, *J. Geophys. Res.*, 109, B03310, doi:10.1029/2002JB002036.

### 1. Introduction

[2] Over the past 20 years, the United States Department of Energy (DOE) has been conducting a feasibility study at Yucca Mountain, in the southwestern part of Nevada, to determine the suitability of this site for a high-level nuclear waste storage facility. The geology at Yucca Mountain consists of heterogeneous layers of fractured volcanic rock [Scott and Bonk, 1984]. The deposition process created layering of welded and nonwelded, partially saturated, tuff layers [Nelson and Anderson, 1992], which show a variable

degree of fracturing and diagenetic alterations [Broxton *et al.*, 1987]. Postdepositional fracturing, the formation of lithophysal cavities, and faulting created a heterogeneous stratigraphy, which is the focus of the feasibility study at Yucca Mountain [Montazer and Willson, 1984; Moyer and Geslin, 1995].

[3] The primary role of geophysical studies at Yucca Mountain has been the measurement and imaging of physical rock properties. Properties such as density, conductivity, bulk, and shear moduli are used to estimate other geologic properties such as stratigraphy, structure, saturation, fracturing, and permeability [Geslin *et al.*, 1994]. Although boreholes and tunnels in the Exploratory Study Facility (ESF) allow direct examination of physical properties, there

is a need to detect and characterize subsurface features away from and between these access points. Boreholes and tunnels to date have given a very small view of the entire repository volume. In addition, the lateral variability and heterogeneity in the Topopah spring formation (the formation of the future repository site) makes it difficult to extrapolate between observation points. For example, the intensely fractured zone encountered in the ESF was not predicted. It is necessary to know the location of significant faults and fracture zones, variation in lithology, and rock type to properly design and predict the performance of the potential repository. It is also necessary to understand how mining activities may affect the integrity and stability of the ESF and potential locations of the repository tunnels. Such questions as the extent of the disturbed zone, rock stability as a function of heating, and the mechanical effect of strong ground motion on the subsurface facilities require seismic data to be properly addressed.

[4] The results of previous surface geophysical work carried out from 1994 through 1996 and reported by *Majer et al.* [1996] suggest that the mountain as a whole is difficult to characterize from the surface because of topography variation, surface noise, near-surface weathering and lithology, and a variety of other access issues. Access to the subsurface in the potential repository horizon is expected to increase spatial resolution as well as directly observe such properties as lithology, fracture, and fault patterns and relating these properties to the seismic results. The ESF tunnel at Yucca Mountain provided the opportunity to carry out a seismic experiment in which the data were collected at depth inside the target formation. The goal of this experiment was to broadly detect and characterize subsurface faults, fracture networks, and lithologic features within the potential repository horizon, the middle nonlithophysal zone (Tptpmn).

[5] Seismic investigations to study the integrity of rock in underground repositories have been carried out in other countries in the past. *Paulsson et al.* [1985] report changes in  $P$  and  $S$  wave velocities, attenuation, and stress of granitic rock during a heater experiment in the Stripa mine facility in Sweden. The Grimsel test site in the central Alps in Switzerland is used as an underground laboratory to study the possibility of nuclear waste storage in granitic rock. Various seismic experiments have been conducted in tunnels and boreholes to determine the best sources for the excitation of high-frequency seismic energy and to investigate fractured crystalline rock over distances of up to 1000 m [*Bühnemann and Holliger, 1998*]. Tomographic imaging studies were performed to determine the location and extent of fractured zones in various host rock. The seismic imaging ranged from small aperture cross-hole studies in the 10 m range [*Vasco et al., 1995*], to larger-scale studies, which combined cross-hole and tunnel geometries across several hundred meters [*Maurer and Green, 1997*].

## 2. Survey Design and Data Acquisition

[6] A series of prototype tests were performed to determine the most suitable types of sources and receivers to image an area of more than 5 km<sup>2</sup> within the repository. After completing the prototype testing, it was decided that vibroseis sources on Yucca Mountain ridge

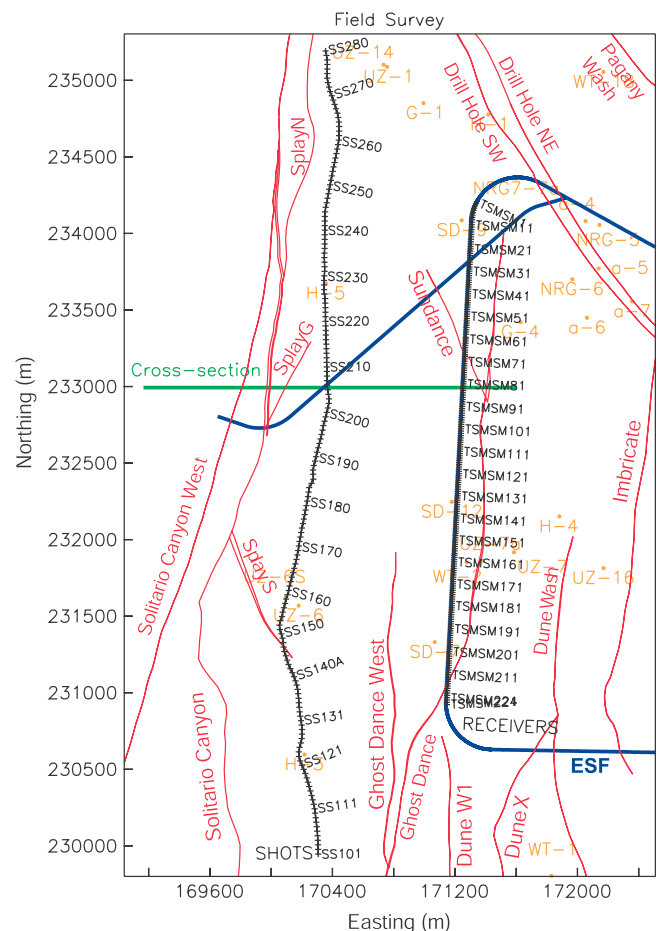


**Figure 1.** Locations of sources and receivers for the full-scale tomography field experiment. The source locations are labeled SS101 to SS280, while the receiver locations are labeled TSMSM101 to TSMSM224. The Exploratory Study Facility (ESF) and cross-drift tunnels are shown in dark blue; major faults are in red, and the two-dimensional (2-D) model cross section is in green. The units of the axes represent Nevada state plane coordinates in meters.

and sensors grouted in shallow holes along the side of the ESF tunnel could provide good data quality at costs within budgetary constraints. In addition to cost constraints, a shutdown of tunnel activities was needed, which only happened at prescheduled times and typically only for two days (over a weekend). Thus a survey was planned that could be completed in two days of acquisition. The prototype data had showed that 30 m source spacing was the minimum required to see coherent waveforms between source locations. Therefore the final survey included 161 sources, which covered over 5 km (at 30 m spacing) along Yucca Ridge. Inside the ESF tunnel, a total of 224 two-component sensors (vertical and horizontal, 448 geophones) with a spacing of 15 m were positioned along the tunnel wall, with the horizontal component normal to the tunnel axis (east-west). The total length of the receiver line was 3345 m. Figure 1 shows the survey geometry in plane view, where source positions are labeled SS101–SS280 along Yucca Ridge and receivers

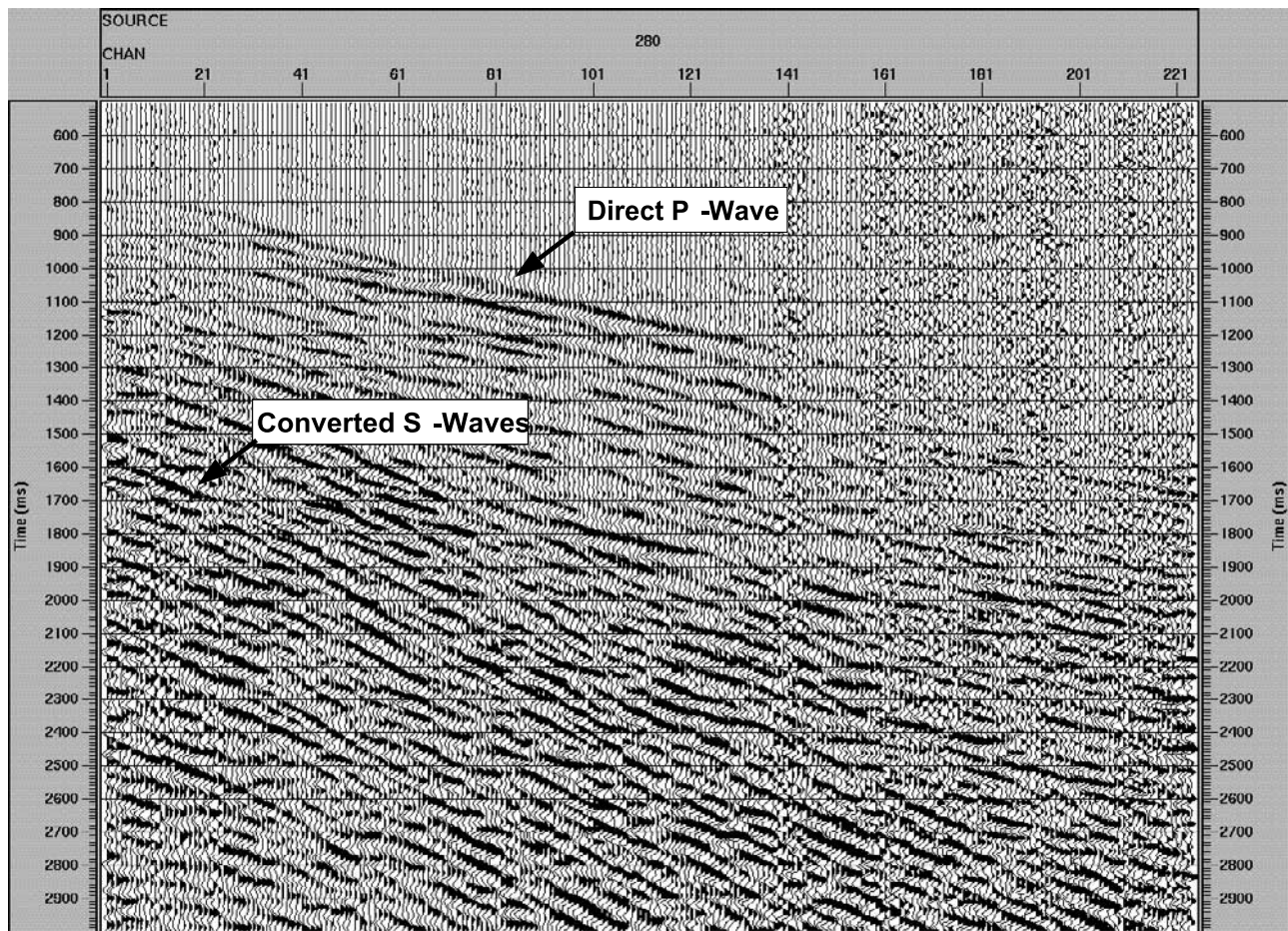


**Figure 2.** Common shot gather of the  $z$  component for source location 280 at the northern end of Yucca Mountain ridge.

TSMSM1–TSMSM224 inside the ESF tunnel. Two vibroseis trucks (30,000 pounds force each) were used in a linear array at each source location. The source signal was a “Varisweep” (to cancel the side lobes) of 12 seconds length from 8 to 60 Hz, repeated 12 times at each source location. The approximate location of the repository area in Figure 1 extends from the receivers in the tunnel westward toward the Solitario Canyon fault. The blue lines represent the main access tunnel (ESF), and the cross drift that starts from the ESF and runs in NE-SW direction through the future repository area and terminates at the western splay of the Solitario Canyon fault.

### 3. Data Processing

[7] The survey produced a total of over 71,000 seismograms. The data were sorted in common shot and receiver gathers. A total of 161 shots were recorded by 224 receivers. A shot gather from a source position located at the northern end of the line along the ridge is presented in Figure 2. The data were bandpass filtered between 20 and 50 Hz, while a notch filter was applied at 60 Hz. A first arrival can be seen for channels 1 through 155, associated with  $P$  waves propagating from the surface to the receivers at depth (as will be shown in the next section). The energy following the direct arrival represents  $P$  to  $S$  converted

waves created near surface interfaces. It can be seen that the amplitudes of the direct  $P$  waves decrease below the noise level for long offsets. This pattern is present in all shot gathers from both ends of the source line, since the attenuation in the medium is too high for waves to propagate from one end of the source line to the opposing end of the receiver line. Therefore far-offset travel times associated with these long travel distances cannot be determined from the data.

[8] The first arrival times were handpicked for each shot gather, resorted to receiver gathers, checked, and then repicked for correct event identification. Event identification is an important step because a complex subsurface structure (such as at Yucca Mountain) can cause the first arriving energy to be associated with different ray paths than those assumed in tomography. To better understand the wave propagation in the current survey, elastic wave equation simulation was needed. Although the geometry of the experiment was three-dimensional (3-D), which suggests the use of 3-D wave propagation modeling, it was not possible to cover the complete survey area because of computational limitations. Therefore it was decided to limit the modeling to vertical sections through the survey area and use 2-D elastic finite difference modeling to gain insight into the nature of arrivals observed in the real data. This decision was supported by the geometry of the geologic units at

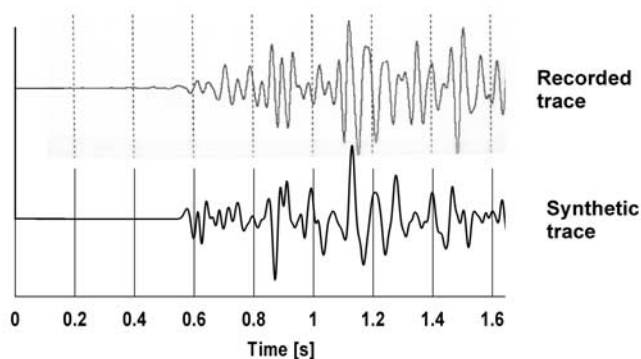


**Figure 3.** Comparison of observed and modeled data for source and receiver positions along the 2-D profile in Figure 1. The synthetic trace was generated with the velocity model shown in Figure 4.

Yucca Mountain, which are predominantly flat as shown in the next section.

#### 4. Numerical Modeling

[9] The first goal in the numerical modeling effort was to understand the propagation path of the waves from the sources on the ridge to the receivers in the tunnel. Therefore as a first step, a 2-D velocity model was created using data from vertical seismic profiling (VSP) recorded in borehole UZ-16, which were projected onto a 2-D cross section of a 3-D site-scale geologic model that was previously derived for Yucca Mountain. The location of UZ-16 and the cross section are given in Figure 1. The geologic site-scale model is well constrained by the numerous borehole measurements throughout the repository area and is used as the standard reference model for

all modeling studies (see Figure 1). The observed seismogram for a source and receiver located along the chosen cross section is given in Figure 3. The initial velocity model derived from the VSP data of UZ-16 was perturbed until a good match between the observed and modeled trace was achieved. The final result is shown in the same figure and reveals a good match for the arrival time and the large amplitudes of the secondary phases. The final velocity model for the selected cross section, shown in Figure 4, is derived by adjusting near surface velocities and applying an exponential velocity gradient across the geologic layers rather than keeping a constant value.

[10] On the basis of the derived velocity model, 2-D wave field snapshot data were generated to understand the nature of wave propagation from the ridge to the tunnel, and to identify the arrivals encountered in the field data. The computed wave fields are shown in Figure 5. The snapshot sequence reveals the location of the wave fronts at various times. The simulation clearly shows that the first arrival energy is traveling almost straight down from the ridge to the repository layer before it refracts horizontally along this high-velocity horizon (refer to Figure 4 for velocity information). The initial vertical wave propagation was caused by very low velocities in the near-surface, while the horizontal wave propagation was caused by the high-velocity middle nonlithophysal zone. This particular wave propagation enabled us to image the desired repository area with a 2-D geometry, because the waves travel through a large volume of the repository horizon horizontally. The images also indicate how *P* wave energy is converted to *S* wave energy in the near-surface layers of the model. The *S* waves built up large amplitudes arriving at later times at the receiver, as seen in the observed data record in Figure 2. In addition to the first arriving waves, a phase should be pointed out that is refracted off the Calico Hills horizon in

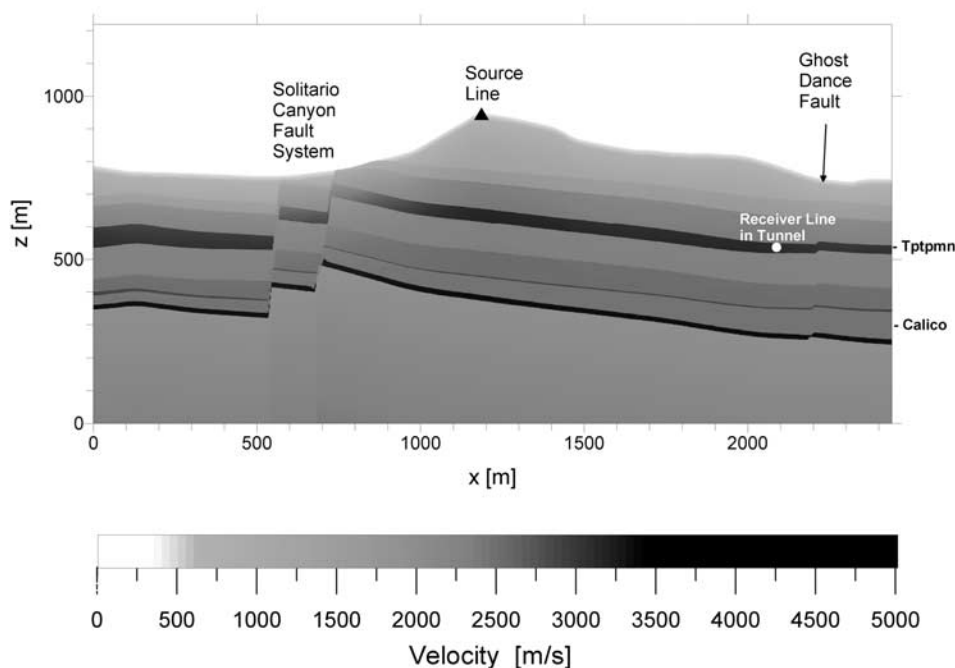


**Figure 4.** Two-dimensional velocity model used for wave equation modeling. The Solitario Canyon and Ghost Dance fault are indicated by offsets in the geologic layering.

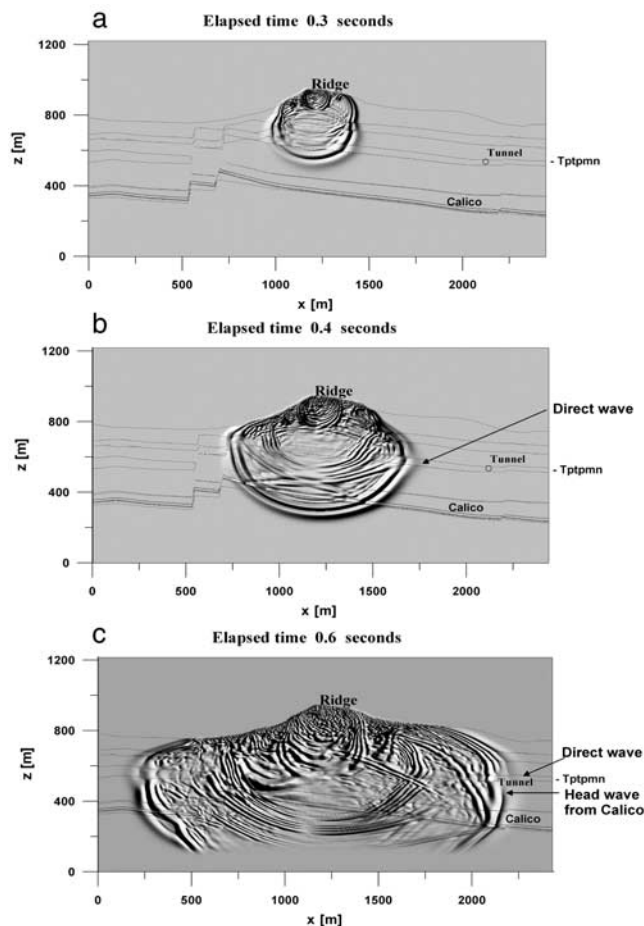


**Figure 5.** Sequential time snapshots of 2-D wave propagation modeling with the velocity model shown in Figure 4. Note that in the 0.3 s frame (Figure 5a), the direct  $P$  wave has already reached the repository horizon with little lateral propagation. At later times the wave continues to propagate along the horizon before it reaches the tunnel. See arrows in Figures 5b and 5c. It is this observation that justifies the use of 2-D tomographic imaging. The head wave from the Calico horizon is indicated in Figure 5c.

the lower part of the model. The refracted wave is indicated by the arrow in Figure 5c.

[11] To model wave propagation from one source across the receiver array, which is perpendicular to the derived velocity model, the receivers were mapped into the plane of the velocity cross section, keeping the distance between source and receivers constant. Such mapping was justified because the used velocity model is laterally homogeneous, and allows us to directly compare move outs of different waves between the synthetic and real data. Figure 6 shows the seismograms of the horizontal components of the receiver array after the mapping procedure. It is evident that at short offsets, the first arriving  $P$  wave has phases that decay at larger offsets. In contrast, the refracted wave from the Calico formation is visible throughout the offset section, and appears to be taking over as first arriving energy after an offset referred to as “merge point” in Figure 6. However, the velocity in the repository horizon is faster than in the

Calico formation below, such that the direct wave remains the first arrival even though its amplitudes are so low that they appear to be passed by the refraction from the Calico formation. Therefore large-offset travel times were not included in the tomographic inversion to avoid incorporating erroneous phase information.

#### 4.1. Zero-Offset Analysis

[12] To have an initial estimate of the variation in seismic wave properties across the tunnel length, data were sorted in a zero-offset geometry, where the sources on the ridge were matched with opposing receivers in the tunnel. A total of 110 traces were found to satisfy this geometry and cover the total length of the geophone array. The traces, aligned along their first arrival travel time, are displayed in Figure 7, where a 200 ms automatic gain control was applied. The first arrivals are aligned at 600 ms across the zero-offset gather. It is evident that there is lateral variation in the amplitudes across the tunnel. To quantify this variation, we determined the root mean square (rms) values of the amplitudes associated with the first arrival. The rms amplitude values were computed in a time window of 80 ms ( $\pm 40$  ms) length (about one wave period) across the first arrival. The resulting values were corrected for geometrical spreading and source statics to account for losses associated with varying propagation distances and source coupling effects along Yucca Ridge, respectively (the static corrections are described in a later section). At this point, the relative amplitudes could be compared across the tunnel length. To support the analysis of this comparison, the fracture density, determined along the tunnel walls, is presented alongside the amplitude values in Figure 8. Both curves are normalized (fracture density to a value of 1, rms amplitudes to a value of 2) to separate them in the plot. It is evident that the correlation is strong, particularly in the sections with increased fracture intensity where the rms amplitudes rise above their background value. This result can be explained by a site amplification caused by a decrease in velocity and density within the fracture zone, or by a guiding effect of the fractures, which keep the propagating waves concentrated within the fracture zone and thus prevent amplitude losses caused by spherical spreading of the waves.

#### 4.2. Noise Study

[13] To test the first hypothesis, we performed a noise investigation. If the increase in seismic amplitudes were caused by site amplification, the noise should be amplified in the same way. Therefore the rms amplitude of the noise was determined over a 0 to 500 ms time window in the zero-offset seismogram section before the onset of the first arrival energy. After normalization of the noise amplitudes, their values are displayed in Figure 8 (upper middle curve). It is clear from this comparison that the noise was not amplified in the same way as the seismic waves, and therefore, site amplification can be ruled out as an explanation for the correlation between the seismic amplitudes and the fracture density. In addition, the static amplitude corrections for the source locations are presented in the upper curve in Figure 8. The trend of the source statics indicates that the correlation could not have resulted from near surface effects, even if the statics had not been removed from the data prior to our analysis. It is therefore

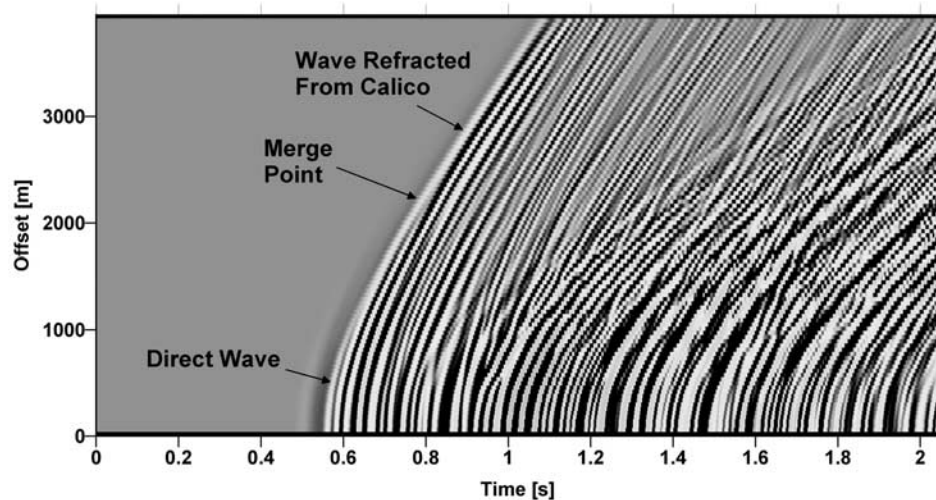


**Figure 6.** Synthetic seismogram of the horizontal components for the receivers in the tunnel after adjustment from 3-D to 2-D geometry. The direct arrival represents a refracted wave across the repository horizon, whereas the second arrival represents a refracted wave across the Calico horizon at depth.

likely that the intensely fractured zone encountered in the tunnel was affecting the seismic amplitudes.

#### 4.3. Wave Propagation in Fractured Zone

[14] To understand the relationship of fracturing and seismic amplitudes, we performed a test to numerically

simulate 2-D elastic wave propagation in a medium containing a fractured zone. The model of the zone consists of a region 910 by 150 m in length with 100 randomly spaced horizontal “fractures.” Each “fracture” is modeled by a low (50%)-velocity discontinuity with a width of one grid point (2.5 m) and a length of 25 m. A point pressure source is

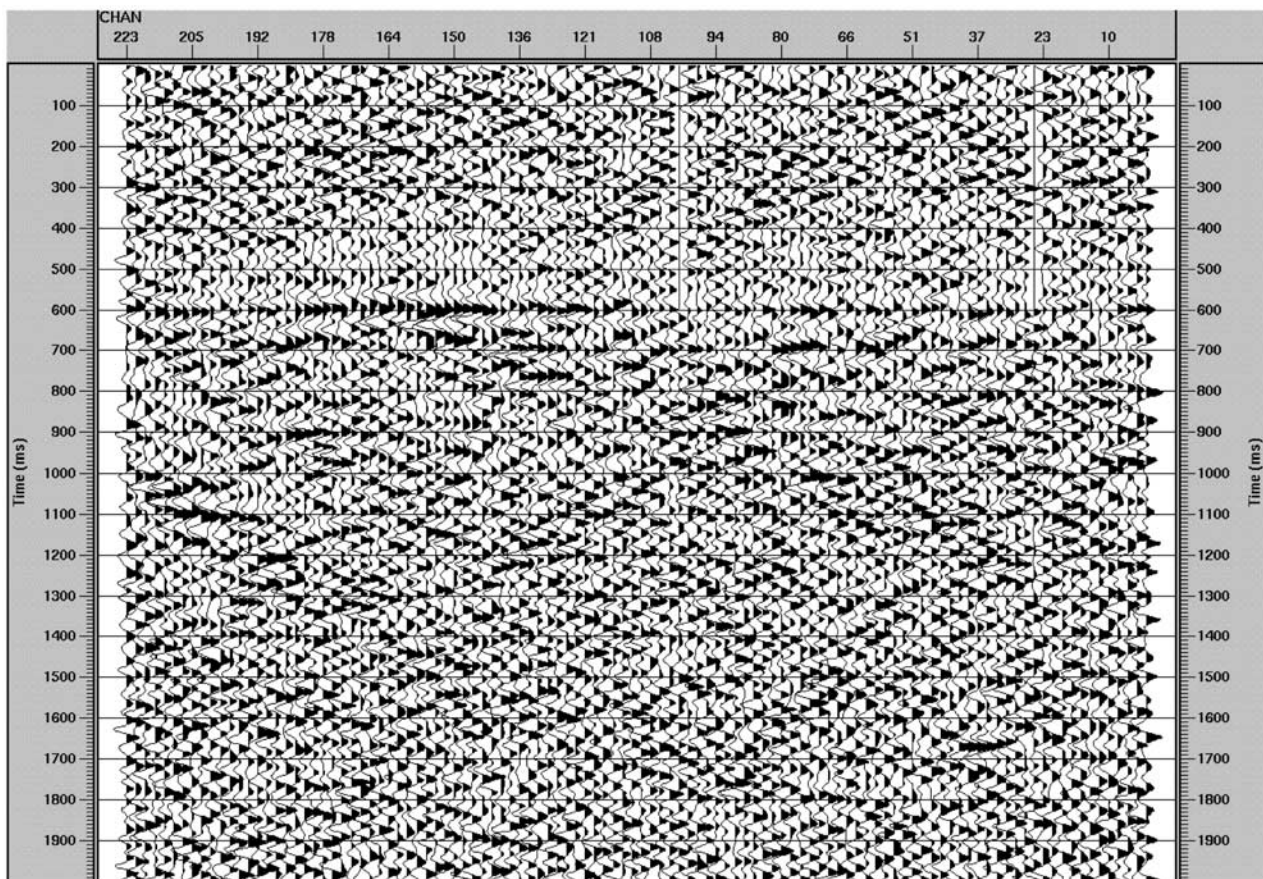


**Figure 7.** Zero-offset gather (z component) for opposing source-receiver pairs in the tunnel. First arrivals are aligned at  $t = 600$  ms.

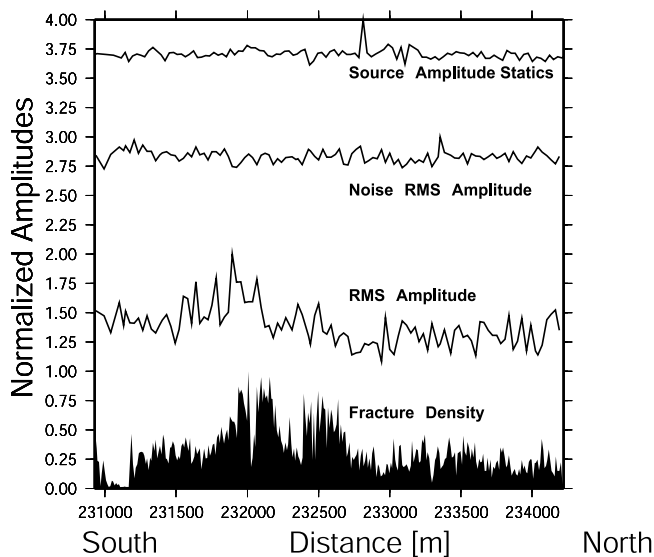


**Figure 8.** Comparison of fracture density in the ESF tunnel with first arrival amplitudes, seismic noise level, and source static amplitude corrections. The coordinates are Nevada state plane in meters. The lower curve shows the fracture density measured inside the tunnel; the lower middle curve shows the RMS amplitude of first arrival zero-offset seismic waves; the upper middle curve shows the RMS amplitude of the 500 ms noise window before arrival of zero-offset seismic waves; and the upper curve shows the source static amplitude corrections along Yucca Ridge.

located at a distance 610 m from the fracture zone (Figure 9a), while an array of 21 observation points, separated by 30 m each, is placed on a vertical profile behind the zone. A 3-D view of the wave field is shown in Figure 9b, where an increase of the field's energy is evident directly behind the fracture zone. An amplitude distribution of the direct wave is presented in Figure 9c. It can be seen that the amplitude high is bounded by regions of low amplitudes on either side. These lows represent energy that propagates obliquely to the fractures (in the  $z$  direction) and is attenuated within this zone. The travel times of the waves, which can be seen in Figure 9d, vary smoothly, revealing negative time shifts, which is also evident in the shading of the wave fronts of the direct arrivals in Figure 9a. It can be concluded that the amplitudes of waves transmitted through a fracture zone form more complicated structures compared to the travel times which exhibit a smoother pattern.

[15] Investigations to study permeability ratios between vertical and horizontal fractures in the repository horizon at Yucca Mountain were conducted by *Sonnenthal et al.* [1997], who concluded that the fracture orientation is predominantly vertical in the northern part of the repository and subhorizontal in the southern region. These subhorizontal fractures are created during the cooling stages of the tuff, when cooling joints formed in horizontal layers that were subsequently filled with gas to form vesicular sheets [Levy et al., 1997; Sweetkind et al., 1997]. These findings could explain the trend of the observed amplitudes along the tunnel wall, which would be guided by the subhorizontal fractures in the southern section of the reservoir and attenuated by vertically aligned fractures in the northern part. The formation of subhorizontal fractures in volcanic

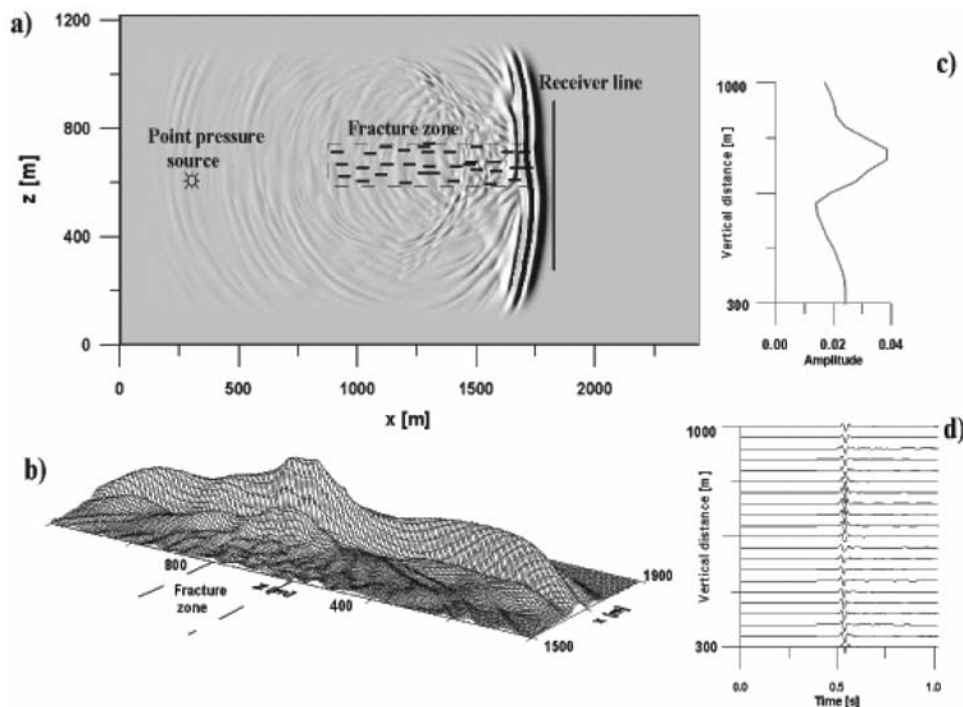


**Figure 9.** Results of elastic wave propagation modeling through a set of horizontal fractures: (a) 2-D model with horizontal fracture zone; (b) 3-D view of wave field behind fracture zone; (c) amplitude values of wave field in Figure 9b; and (d) individual waveforms.

rocks is not limited to Yucca Mountain; similar observations have been reported by *McMillan et al.* [1997] for the Columbia River flood basalts.

## 5. Tomographic Imaging

### 5.1. Source Projection at Depth

[16] The numerical modeling in the last section indicated that the elastic waves propagate downward at a steep angle toward the repository horizon (Tptpmn), after which they are refracted and propagate along this interface. To account for this wave propagation, it was necessary to project the source locations from the surface onto the top of the Tptpmn layer at depth for two-dimensional tomographic imaging to be applicable. Therefore ray tracing was performed based on the 2-D velocity model derived in the last section, to estimate the projected source locations on the Tptpmn layer and to determine the associated travel time corrections. It was found that the rays for all source positions had steep takeoff angles between  $87^\circ$  and  $89^\circ$ . The travel time corrections for the downward projection of the sources were estimated by an inverse scheme as presented in the next section.

### 5.2. Static Corrections

[17] Previous results from VSP and surface seismic experiments [*Majer et al.*, 1996] indicate that seismic velocities in the shallow subsurface at Yucca Mountain are very low and heterogeneous, caused by weathering, tectonic, and other geologic processes. In addition, the exposed rocks on Yucca Ridge experience much lower confining pressures, which allows microcracks to open and lowers their velocities even more. It is quite common that the upper parts of the subsurface develop strong velocity gradients that can be found even in solid rocks like granite. Furthermore, the heterogeneity in the shallow subsurface causes the coupling of seismic sources to vary along the source line. Therefore these effects need to be removed from the data during the projection of the sources onto the repository horizon before further processing can be done. For our studies, the standard practice of near-surface (or near-borehole) static corrections was extended to include a correction for all propagation effects encountered by the waves between ridge and the horizon at depth. This is done by using a least squares regression fit to the travel time data. Because the present case consists of nonuniform amounts of data points for different source locations (each source location yielding a varying number of first arrival times), weighting coefficients are introduced in the minimization function of the inverse problem. (The derivation of the applied least squares approach is presented in Appendix A.) The estimated travel time correction associated with the projection of the sources to depth are presented in Figure 10. The slight increase in static times from the southern to the northern end of the source line on Yucca Mountain ridge, is in agreement with a decrease in velocity along the ridge from south to north observed in previous VSP studies [*Majer et al.*, 1996]. In addition to the source statics, receiver static corrections were applied to account for inhomogeneities in the vicinity of the ESF tunnel, which may introduce anomalous velocity structures in the inversion results. After the data set has been corrected for static

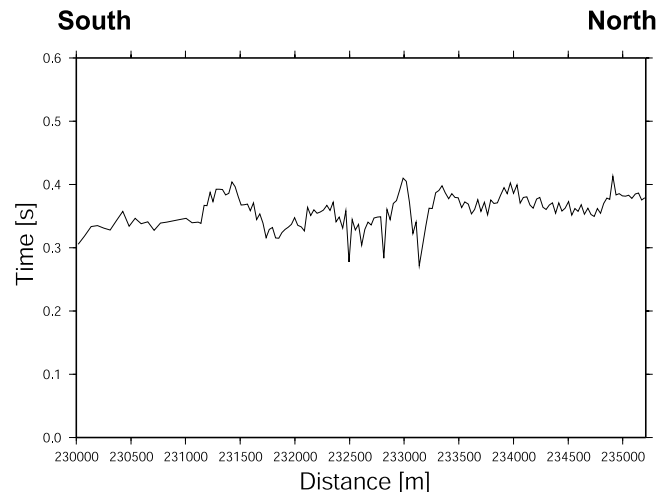


**Figure 10.** Static travel time corrections for mapping the source locations from Yucca Ridge to the repository horizon at depth. The coordinates are Nevada state plane in meters.

time variations, tomographic imaging of the horizon was performed. Static corrections of source and receiver locations are a common approach, when adjustments to stations have to be made in space and time, or when the correct locations of the stations need to be determined during the inversion process [*Maurer and Green*, 1997].

### 5.3. Appraisal of the Travel Time Inversion Results

[18] On the basis of the lessons learned from the numerical modeling examples, the travel times of the first-arriving waves were handpicked for all common source gathers, resorted to common receiver gathers, and repicked to verify the event identification. This process resulted in a total of over 40,000 travel times out of 71,000 possible traces. The inversion of the travel times was performed in a two-step approach, where the forward modeling was based on a 2-D eikonal solver [*Podvin and Lecomte*, 1991], while the inversion was based on curved ray algebraic reconstruction technique (ART) [*Peterson et al.*, 1985]. Before the inversion estimates are closer interpreted, they will be appraised to determine the misfit and resolution.

[19] The inversion process was based on a homogeneous starting model for which travel times  $t^{\text{pre}}$  are calculated along rays for each source-receiver combination. The differences  $\delta t$  between the observed  $t^{\text{obs}}$  and the calculated  $t^{\text{pre}}$  travel times are subsequently backprojected along the rays and the starting model is updated. This process is repeated until the misfit is reduced to a sufficiently low level and a smooth model is obtained.

[20] The results of the travel time inversion are presented in Figure 11. To evaluate whether the model in Figure 11 can be resolved with the current approach and the given source-receiver geometry, theoretical travel times were calculated for wave propagation from the sources to the receivers through the model in Figure 11. The theoretical travel times were subsequently inverted using the approach described above in an attempt to recover the model in Figure 11. The result of this inversion is shown in Figure 12a. It can be seen that the features of the model are recovered in magnitude and space. To appraise the

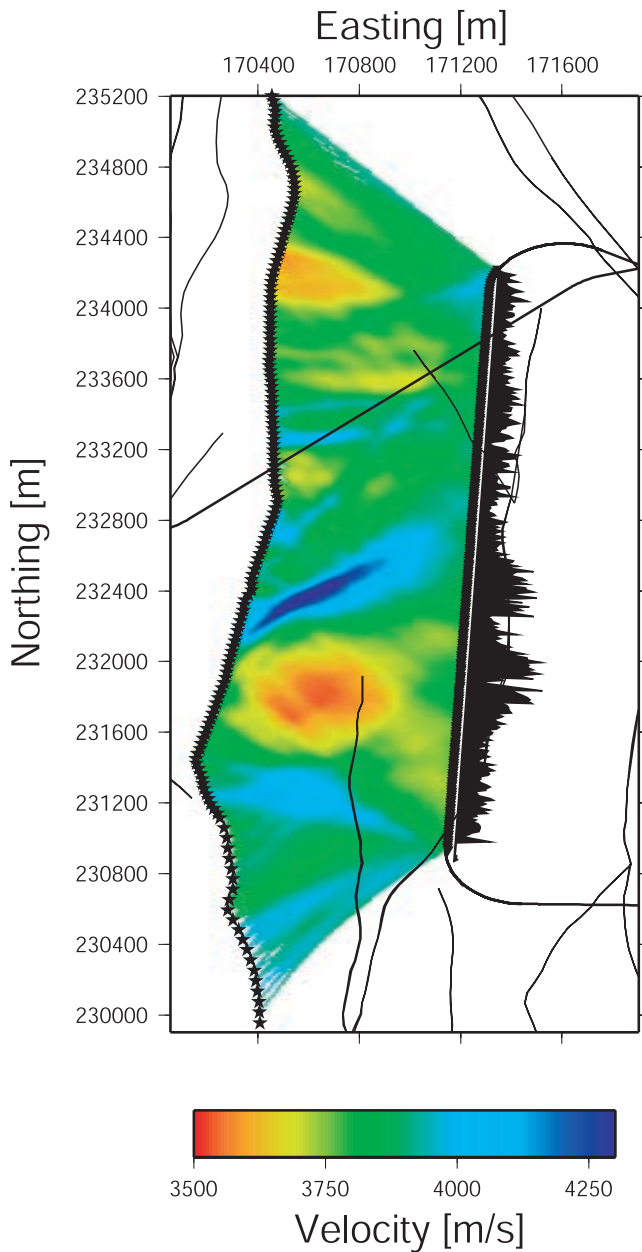


**Figure 11.** Velocity estimates of the repository horizon based on curved ray travel time inversion. Prior to inversion the travel times have been corrected for static shifts associated with local anomalies in the vicinity of sources and receivers. The ESF and cross-drift tunnels and major faults are drawn as black lines, and the fracture density measured in the ESF tunnel is displayed for better comparison of the results. The coordinates are Nevada state plane in meters.

inversion result for this noise free data set, we calculate the relative misfit between the observed  $t_i^{\text{obs}}$  and the calculated  $t_i^{\text{pre}}$  travel times as

$$\sigma = \frac{\sqrt{\sum_i^N (t_i^{\text{pre}} - t_i^{\text{obs}})^2}}{\bar{t}},$$

where  $N$  is the number of rays and  $\bar{t}$  is the average travel time defined as

$$\bar{t} = \frac{\sum_i^N t_i^{\text{obs}}}{N}.$$

The relative misfit for the estimate in Figure 12a is shown in Figure 12b. Because the data were noise free the damping was kept at a minimum and the relative misfit was reduced to less than 0.04%. Thus it can be stated that for noise free data the model in Figure 11 can be recovered practically error free with the current approach.

[21] The actual travel time data, on the other hand are not noise free, because of picking errors introduced during the determination of the travel times. The actual maximum picking error in the data is estimated to be 20 ms, or one quarter cycle of the incident wave. Therefore the numerical exercise is repeated introducing a random error of 20 ms of white uncorrelated noise to the theoretical travel times. The inversion result of the noise contaminated data is shown in Figure 12c. It is evident that the overall magnitude of the estimates is reduced and less smooth than in the case of noise free data. At the same time the misfit for this inversion result has increased to approximately 3.7% after 20 iterations (see Figure 12d). The lack of smoothness of the estimates in Figure 12c indicates that further iterations to decrease the misfit would increase the roughness of the model and degrade the inversion result.

[22] The numerical exercise demonstrated the applicability of the current inversion method to the problem at hand, while it revealed its limitations in the presence of noise. With these results in mind, we will appraise the inversion results of the travel time data presented in Figure 11.

[23] The misfit of the estimates in Figure 11 is presented in Figure 13a. After 20 iteration steps, it has been reduced to 3.4%, and thus lies below the noise level of the data as shown in Figure 12d. The resolution of the estimates for algebraic reconstruction methods is best evaluated by the number of rays in a given pixel, which contribute to the estimate of that pixel. A sufficient number of rays particularly over a large area of adjacent pixels is indicative of a well resolved estimate, whereas a low ray count may lead to less resolved estimates. Figure 13b shows the ray density for the previous inversion result. It can be seen that in the south central area the ray density is high with values between 100 and 200 rays per cell. In contrast, the southern most and northern end of the survey area reveal a lower ray density with values between 50 and 100 rays per cell. The relatively homogeneous and high ray density in the south central area will produce estimates that are well resolved with the current inversion scheme.

[24] In summary, it can be stated that the inversion result in Figure 11 represents a model that can explain the travel time data with accuracy that is limited by the noise in the time picks.

#### 5.4. Interpretation of the Travel Time Inversion Results

[25] For a better comparison between the inversion results and the fracture intensity observed along the tunnel walls in the ESF, the graph of the fracture density is displayed next to the velocity estimates in Figure 11. Among the main

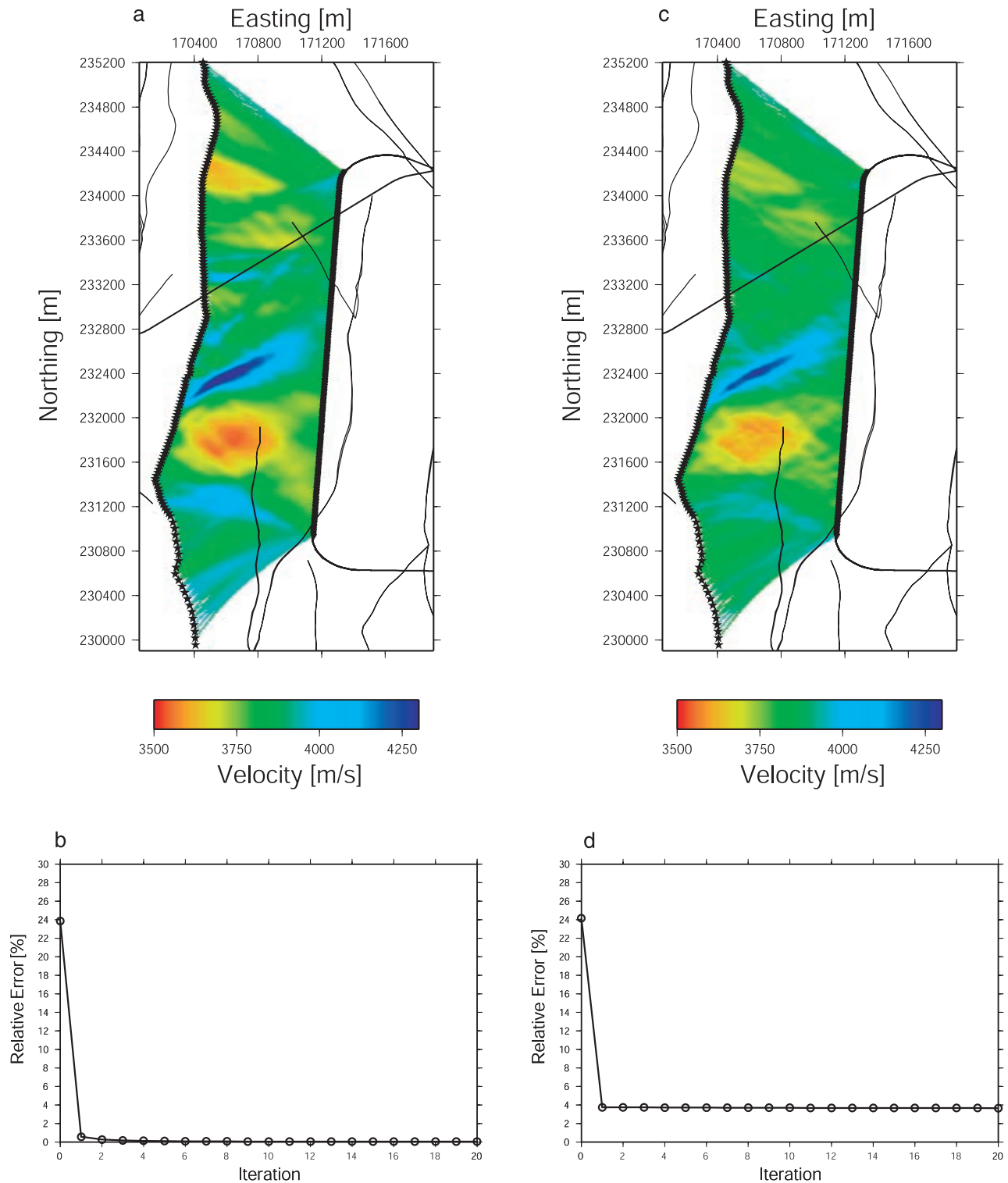


**Figure 12.** (a) Velocity estimates of the repository horizon based on numerical travel times calculated for the model in Figure 11. (b) Relative error between the calculated and observed travel times for the travel time inversion in Figure 12a. (c) Velocity estimates of the repository horizon based on numerical travel times including random noise calculated for the model in Figure 11. (d) Relative error between the calculated and observed travel times for the travel time inversion in Figure 12c.

features observed in the repository is the broad velocity low in the south central area of the image (at about 231800 N). This velocity low appears to extend northeast and southwest toward the ESF although the velocity decrease is less

pronounced in these areas. The reason could be the application of static receiver corrections. The receiver statics, displayed in Figure 14, show positive values throughout the southern section of the tunnel. Because the statics are

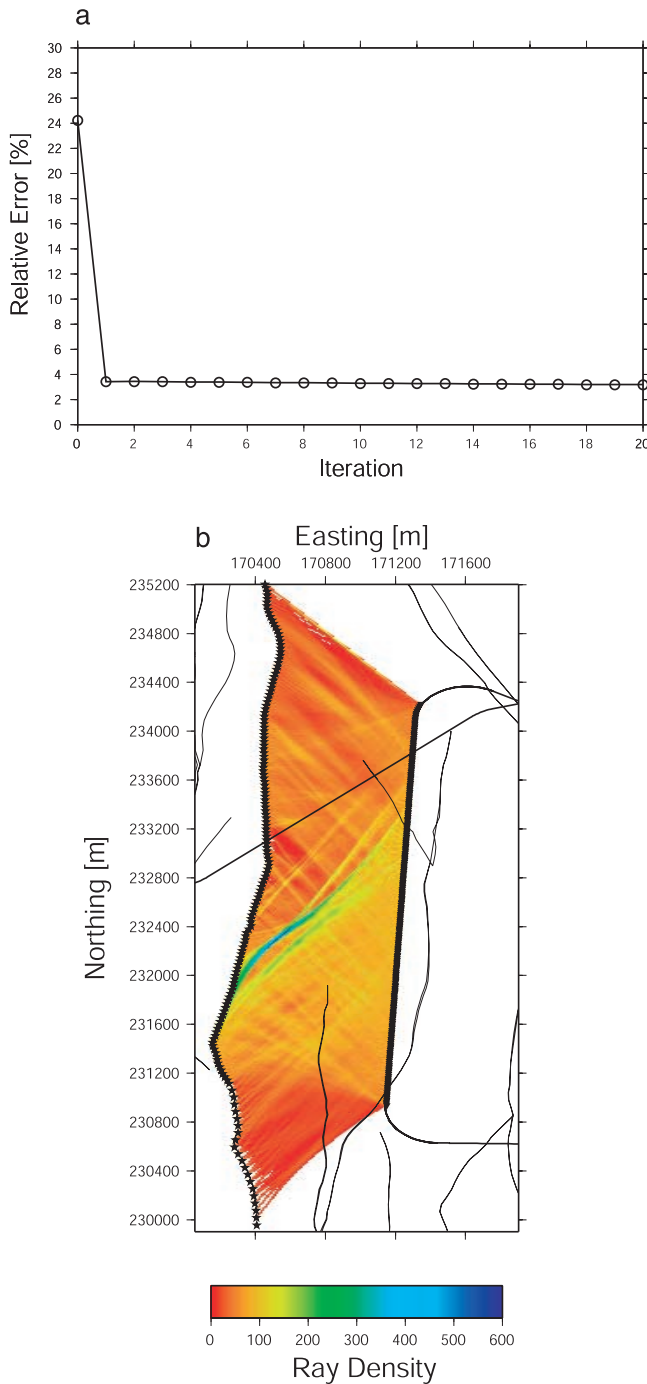


**Figure 13.** (a) Relative error between the calculated and observed travel times for the inversion in Figure 11. (b) Ray density plot for the inversion result in Figure 11.

subtracted from the travel times they will diminish the effect of low velocity anomalies in close proximity to the tunnel. In contrast to the south, the northern part of the repository appears more homogeneous. The main anomalous zone, a low-velocity feature at the western margin of the survey area (at about 234200 N) is likely an artifact of the low ray coverage in this area (see Figure 13b). The inversion tends to shift high or low estimates to areas that are less constrained as in the case of low ray density.

[26] The narrow velocity high in the central area trending from 232000 N in northeastern direction is collocated with the highest ray density as shown in Figure 13b. To test whether this feature is an artifact, we perform an inversion based on straight rays, which provides a more homogeneous ray coverage and avoids clustering of bending rays. The estimates of the straight ray inversion are shown in Figure 15a. It can be seen that the image shows strong similarity to the curved inversion result in Figure 11. The high-velocity ridge is located in the same area, although it appears somewhat broader, because the straight rays are not refracted into this region. This feature appears to be real and could possibly indicate an area of high stress that may cause fractures to close and the velocity to increase over the background values. The misfit of the straight ray inversion is shown in Figure 15b. The reduction is similar to that of the curved ray inversion (see Figure 13a) with a misfit reduction to approximately 3.25% after 20 iteration steps.

[27] The similarity between straight and curved ray inversion has been observed before, particularly in the case where the medium consists of uniform rock or soil type with velocity variations of less than 40% [Peterson, 1986]. The situation of the repository at Yucca Mountain represents such a case.

### 5.5. Fracture-Density Estimation

[28] In an attempt to quantify the fracture properties of the repository, we used a derivation based on effective media theory [O'Connell and Budiansky, 1974]. This model is a low-frequency approximation and appropriate for wavelengths much longer than the fracture dimensions. Thus it is appropriate to apply it to Yucca Mountain, where the wavelengths are on the order of 150 m and the fracture dimensions are in the meter range. The model combines seismic  $P$  and  $S$  wave velocities, fracture density, matrix properties, and fluid saturation. This approximation was successfully applied to the UZ-16 VSP data to derive the saturation and fracture density profile [Kaelin, 1998], but unlike the ESF, UZ-16 had no confirmation of large-scale fracture density that was affecting seismic wave propagation within the wavelengths generated by the VSP. The accuracy

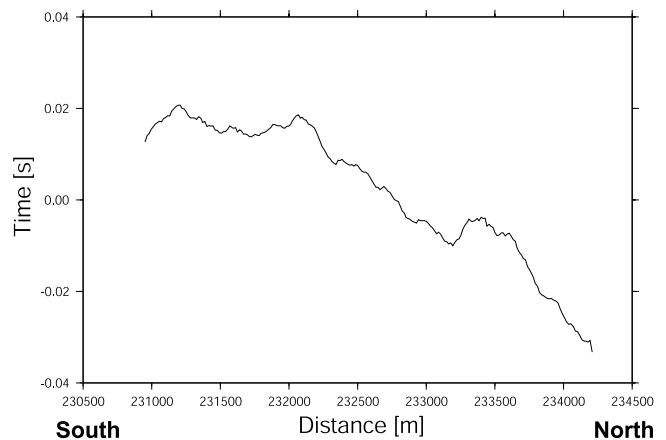


**Figure 14.** Static travel time corrections for the receiver locations along the ESF tunnel. The coordinates are Nevada state plane in meters.

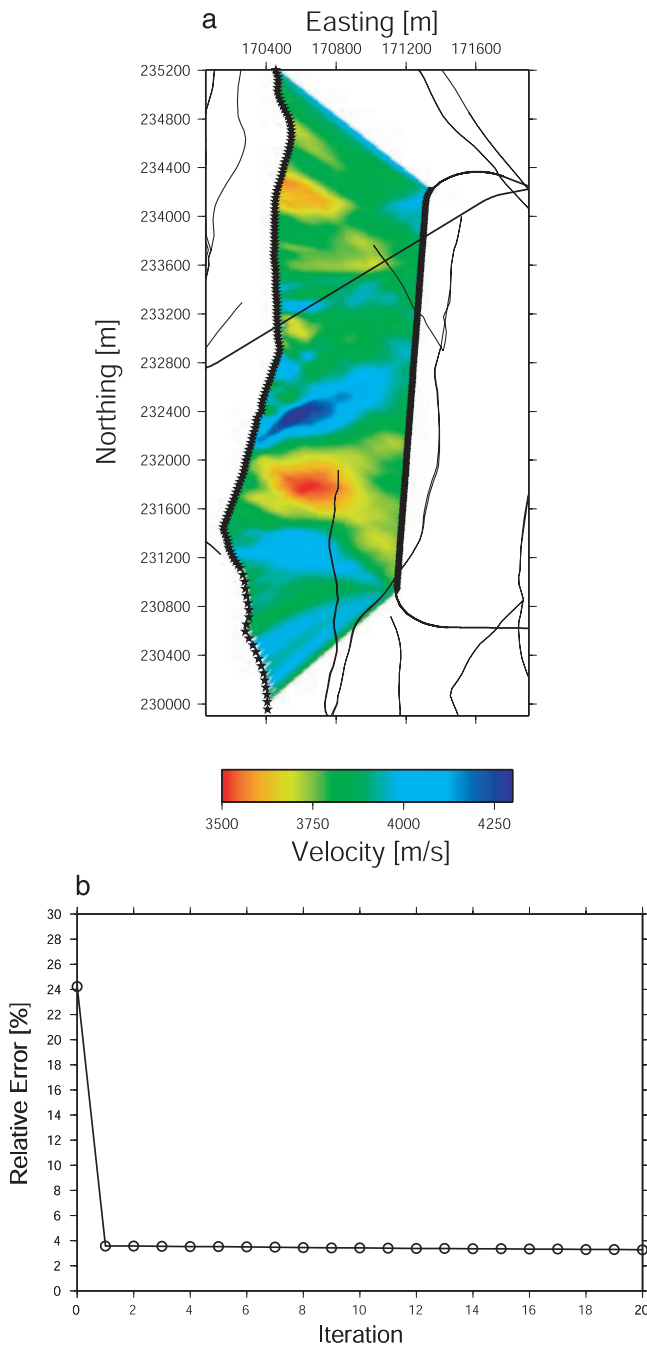


**Figure 15.** (a) Velocity estimates of the repository horizon based on straight ray travel time inversion. (b) Relative error between the calculated and observed travel times for the straight ray travel time inversion in Figure 15a.

of the results at UZ-16 demonstrated the applicability of the theory to the repository nonlithophysal and lithophysal zones. The fracture density  $\epsilon$  is defined as

$$\epsilon = \left( \frac{2N}{\pi} \right) \left( \frac{A^2}{P} \right),$$

where  $N$  represents the number of cracks per unit volume,  $A$  the area of the crack, while  $P$  is the crack perimeter.

Furthermore, for a partially saturated fractured medium, the fracture density is given by

$$\epsilon = \frac{45}{16} \left( \frac{\nu_s - \bar{\nu}_s}{1 - \bar{\nu}_s^2} \right) \frac{(2 - \bar{\nu}_s)}{[(1 - \xi)(1 + 3\nu_s)(2 - \bar{\nu}_s) - 2(1 - 2\nu_s)]},$$

where  $\xi$  represents fracture saturation,  $\nu_s$  is the Poisson ratio of the unfractured matrix, and  $\bar{\nu}_s$  is the Poisson ratio of the effective matrix. The two equations can be combined to solve for the number of cracks ( $N$ ) per unit volume.

[29] Unlike the data from UZ-16, there are many assumptions used to derive the relationship for the repository horizon. The following values are taken from geologic and geophysical studies of the repository horizon [Buesch *et al.*, 1996; Majer *et al.*, 1996] or from matrix properties of cores from UZ-16: an average Poisson's ratio of 0.34 for the unfractured matrix, an average crack saturation of 60%, an  $S$  wave velocity of 2150 m/s ( $S$  waves arrival times are not identified from the data). It is also assumed that all porosity is fracture porosity (total porosity in the repository horizon is about 10%) and that the fractures have an average dimension of 1 m<sup>2</sup>. Although these properties vary throughout the imaged volume, the above values are kept fixed because it is not intended to include other laterally varying properties within the scope of this work. Further refinements of the fracture density could be obtained by more accurate values of saturation,  $S$  wave velocity, and matrix properties.

[30] The information in the velocity tomogram is the basis for the fracture density mapping shown in Figure 16. It is evident that the mapping and the values observed in the ESF and cross drift match quite well, even in their absolute values. In the south central region of the repository, the results of the fracture density mapping suggest that the intensely fractured zone, encountered in the ESF, extends in southwestern direction throughout most of the repository horizon. Although it appears that the fracturing is reduced in the vicinity of the ESF, it can be expected that the fractured zone extends closer toward the tunnel, because the application of receiver statics reduced the effect of the fractures in the inversion process.

[31] In the northern part along the cross drift, the estimated fracture density increases in the central section of the tunnel, which matches the observed values. Overall the northern section of the repository appears less fractured, as confirmed during the excavation of the cross drift.

[32] The results indicate that the fracture density model of O'Connell and Budiansky [1974] is a good approximation for the application of seismic wave propagation in the repository horizon and validates the choice of parameters above. Furthermore, the results provide some confidence that seismic velocities correlate closely to fracture properties.

## 6. Conclusions

[33] These studies have demonstrated the potential of large-scale, surface-to-tunnel, seismic tomography at Yucca Mountain. Numerical modeling helped to develop novel techniques to maximize seismic imaging and produce interpretable results for over 5 km<sup>2</sup> of the repository horizon.

[34] The zero-offset relative amplitude distribution revealed surprising results, in that the amplitudes increased

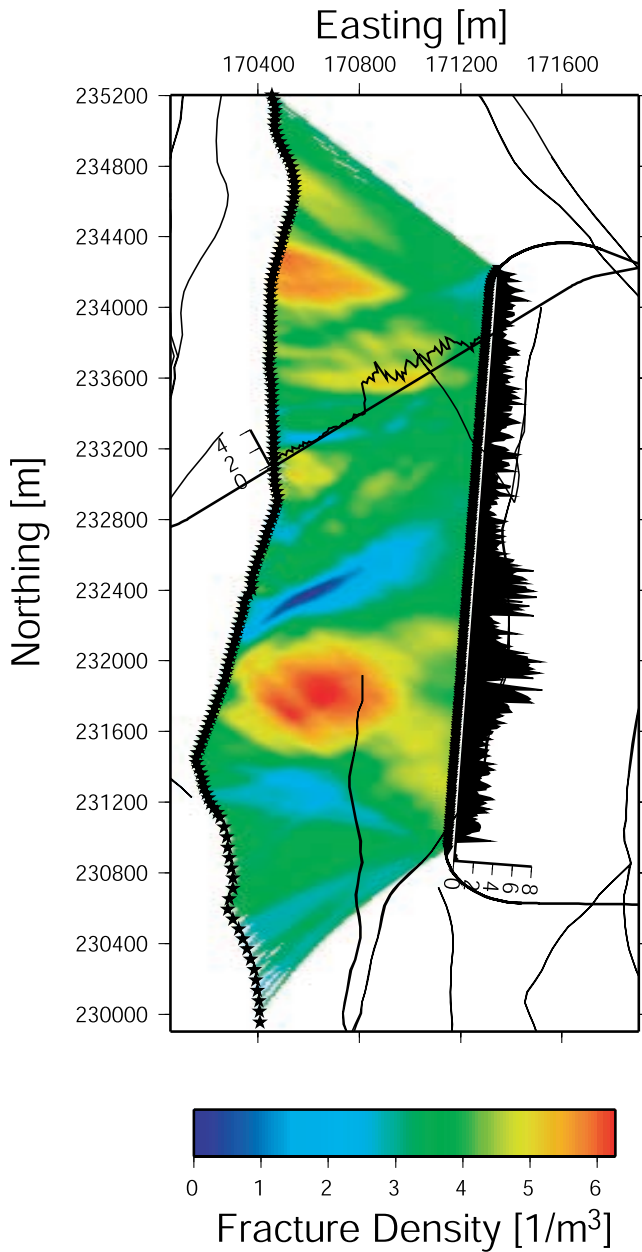


**Figure 16.** Fracture density image of the repository horizon. The magnitudes of the fracture density estimates have not been normalized. The tomographic fracture estimates are based on an average fracture dimension of  $1 \text{ m}^2$ , while the measured fracture densities in the ESF and cross drift are based on fracture lengths of 1 m or longer. The fracture scales next to ESF and cross-drift histograms show the number of fractures per meter along the tunnel walls.

in regions of high fracture intensity. Because site amplification effects can be excluded, one possible explanation could be that the horizontal fractures are guiding energy during propagation, producing constructive interference and causing an increase in amplitude rather than the decrease that one would expect for a highly fractured zone. Initial modeling exercises confirmed the possibility of fractures inducing this result. Whether this

effect is more likely for subhorizontal or vertical fractures needs investigation, but this observation holds the promise of more accurately imaging similar fracture zones.

[35] The interpretation of the velocity images was purely based on fracturing. It is possible that there are different physical processes at work within the large imaged region. Properties such as saturation, spatially varying velocity anisotropy, or varying lithophysal content can combine to create the observed heterogeneity. The produced images can be interpreted as follows.

[36] 1. It can be assumed that velocity variation within an individual formation is a good indication of fracture content. Broad regions of high velocity indicate relatively unfractured rock, such as in the blue areas of the velocity tomogram north of the highly fractured zone. This feature could possibly indicate an area of high stress that may cause fractures to close and the velocity to increase over the background values.

[37] 2. Broad regions of low velocity indicate relatively fractured rock, such as in the south central region and along the southern end of the ESF.

[38] 3. Subsurface faults and associated fracture zones may be defined by linear features in the velocity tomograms. However, such features were not encountered in this study. One reason could be lack of resolution as the wavelength of the seismic waves is on the order of 150 m, while the width of the Ghost Dance fault encountered in the ESF was only 0.5 m. However, a zone of fracturing surrounding a fault might well be detectable by travel time inversion methods.

[39] 4. The overall nature of the repository horizon appears heterogeneous with maximum velocity variations of 10% from homogeneous background values. It should be noted that because of the seismic wavelength, the tomographic images include effects from the upper-lithophysal and lower-lithophysal horizons above and below the current repository, and that these zones also affect the observed heterogeneity.

## Appendix A

[40] In the following, the equations used for the static corrections during the relocation of the sources are presented. It was stated in the text that the static effects on travel time must be accounted for, before the data set can be used for tomographic inversions. Similarly, the effects of near surface amplitude variations needed to be corrected, before the data were used for zero-offset amplitude analysis along the tunnel. The corrections are done using a least squares regression fit to travel time and amplitude data [Robinson, 1981]. However, since the present case consists of nonuniform data points for each source position (for most source positions longer offset travel times cannot be determined), weighting coefficients are introduced in the minimization function of the inverse problem. The following data model is assumed:

$$u_{ij} = c_i + pr_{ij} + n_{ij},$$

where the indices  $i$  and  $j$  indicate source and receiver positions, respectively,  $r_{ij}$  is the distance from the  $i$ th source

to the  $j$ th receiver, and  $n_{ij}$  is random noise. For the case of travel times, it follows that

$$u_{ij} = t_{ij}, c_i = t_i, p = \frac{1}{v_0},$$

where  $t_{ij}$  are the travel time picks,  $t_i$  are the source static time corrections, and  $v_0$  is the background velocity. For the case of amplitudes, it follows that

$$u_{ij} = \ln(A_{ij}), c_i = \ln(A_i), p = -\alpha_0,$$

where  $A_{ij}$  are the amplitudes associated with the first arrivals,  $A_i$  are the source static amplitude corrections, and  $\alpha_0$  is the background attenuation coefficient.

[41] The function

$$S = \sum_{ij} (u_{ij} - c_i - pr_{ij})^2 a_{ij}$$

is minimized, where  $a_{ij}$  represent the weighting coefficients, which are chosen as  $a_{ij} = 0$  for missing data and  $a_{ij} = 1$  for all other data points. The static corrections  $c_i$  as well as the background parameter  $p$  are assumed to be unknown. The LSQR solution of the problem has the form

$$\hat{p} = \sum_{ij} r_{ij} a_{ij} \left( u_{ij} - \frac{\sum_i u_{ij} a_{ij}}{\sum_i a_{ij}} \right) \left( \sum_{ij} r_{ij} a_{ij} \left( r_{ij} - \frac{\sum_i r_{ij} a_{ij}}{\sum_i a_{ij}} \right) \right)^{-1}$$

$$\hat{c}_i = \frac{1}{\sum_j a_{ij}} \sum_j (u_{ij} - \hat{p} r_{ij}) a_{ij},$$

where  $\hat{p}$  is the estimate of the background slowness or attenuation, and  $\hat{c}_i$  is the estimate for the source time or source amplitude static corrections, for the case of travel time or amplitude data, respectively. The advantage of the equations above is that they allow to solve for the static corrections analytically, such that an inversion of large matrices can be avoided.

[42] **Acknowledgments.** The authors would like to acknowledge reviews by Lane Johnson, Donald Vasco, Kenneth Williams, Daniel Hawkes, Alberto Michelini, and two anonymous reviewers, whose helpful comments and suggestions improved the content of this paper. We would also like to thank Daniel O'Connell for the use of his eikonal solver. This work was supported by the Department of Energy's Office of Energy Research Basic Energy Sciences Geoscience Program under contract DE-AC03-76SF00098 at Berkeley Laboratory's Center for Computational Seismology and Geophysical Measurement Center.

## References

- Broxton, D. E., D. L. Bish, and R. G. Warren (1987), Distribution and chemistry of diagenetic minerals at Yucca Mountain, Nye County, Nevada, *Clays Clay Miner.*, 35(2), 89–110.
- Buesch, D. C., R. W. Spengler, T. C. Moyer, and J. K. Geslin (1996), Proposed stratigraphic nomenclature and macroscopic identification of lithostratigraphic units of the Paintbrush group exposed at Yucca Mountain, Nevada, *U.S. Geol. Surv. Open File Rep.*, 94-469, 47 pp.
- Bühnemann, J., and K. Holliger (1998), Comparison of high-frequency seismic sources at the Grimsel test site, central Alps, Switzerland, *Geophysics*, 63(4), 1363–1370.

- Geslin, J. K., T. C. Moyer, and D. C. Buesch (1994), Summary of lithostratigraphic logging of new and existing boreholes at Yucca Mountain, Nevada, August 1993 to February 1994, *U.S. Geol. Surv. Open File Rep.*, 94-342, 39 pp.
- Kaelin, B. (1998), Seismic imaging of the shallow subsurface with high frequency seismic measurements, Ph.D. thesis, *LBNL Rep. 42058*, Univ. of Calif., Berkeley.
- Levy, S. S., D. S. Sweetkind, J. T. Fabryka-Martin, P. R. Dixon, J. L. Roach, L. E. Wolfberg, D. Elmore, and P. Sharma (1997), Investigation of structure controls and mineralogical associations of chlorine-36 fast pathways in the ESF, *Milestone Rep. SP2301M4, LA-EES-1-TIP-97-004*, 39 pp., Los Alamos Natl. Lab., Los Alamos, N. M.
- Majer, E. L., M. A. Feighner, L. R. Johnson, T. M. Daley, E. Karageorgi, K. H. Lee, K. H. Williams, and T. V. McEvilly (1996), *Surface Geophysics, Yucca Mountain Project*, vol.1, *Synthesis of Borehole and Surface Geophysical Studies at Yucca Mountain, Nevada and Vicinity*, *Milestone Rep. OB05M*, 71 pp., Lawrence Berkeley Natl. Lab., Berkeley, Calif.
- Maurer, H. R., and A. G. Green (1997), Potential coordinate mislocations in crosshole tomography: Results from the Grimsel test site, Switzerland, *Geophysics*, 62(6), 1696–1709.
- McMillan, K., R. W. Cross, and P. E. Long (1997), Two-stage vesiculation in the Cohasset Flow of the Grande Ronde Basalt, south-central Washington, *Geology*, 15(9), 809–812.
- Montazer, P., and W. E. Willson (1984), Conceptual hydrologic model of flow in the unsaturated zone, Yucca Mountain, Nevada, *U.S. Geol. Surv. Water Resour. Invest. Rep.*, 84-4355, 55 pp.
- Moyer, T. C., and J. K. Geslin (1995), Lithostratigraphy of the Calico Hills formation and Prow Pass Tuff (Crater Flat Group) at Yucca Mountain, Nevada, *U.S. Geol. Surv. Open File Rep.*, 94-460, 59 pp.
- Nelson, P. H., and L. A. Anderson (1992), Physical properties of ash flow tuff from Yucca Mountain, Nevada, *J. Geophys. Res.*, 97, 6823–6841.
- O'Connell, R. J., and B. Budiansky (1974), Seismic velocities in dry and saturated cracked solids, *J. Geophys. Res.*, 79, 5412–5426.
- Paulsson, B. N. P., N. G. W. Cook, and T. V. McEvilly (1985), Elastic-wave velocities and attenuation in an underground granitic repository for nuclear waste, *Geophysics*, 50(4), 551–570.
- Peterson, J. E. (1986), The applications of algebraic reconstruction techniques to geophysical problems, Ph.D. thesis, Univ. of Calif., Berkeley.
- Peterson, J. E., B. N. Paulson, and T. V. McEvilly (1985), Applications of algebraic reconstruction techniques to cross hole seismic data, *Geophysics*, 50(10), 1566–1580.
- Podvin, P., and I. Lecomte (1991), Finite difference computation of travel times in very contrasted velocity models: A massively parallel approach and its associated tools, *Geophys. J. Int.*, 105, 271–284.
- Robinson, E. A. (1981), *Least Squares Regression Analysis in Terms of Linear Algebra*, Goose Pond Press, Houston, Tex.
- Scott, R. B., and J. Bonk (1984), Preliminary geologic map of Yucca Mountain, Nye County, Nevada, with geologic sections, *Rep. OFR-84-494*, 9 pp., U.S. Geol. Surv., Denver, Colo.
- Sonnenthal, E. L., C. F. Ahlers, and G. S. Bodvarsson (1997), Fracture and fault properties for the UZ site-scale flow model, in *The Site-Scale Unsaturated Zone Model of Yucca Mountain, Nevada, for the Viability Assessment*, edited by G. S. Bodvarsson, T. M. Bandurraga, and Y. S. Wu, *Rep. LBNL-40376*, chap. 7, pp. 1–34, Lawrence Berkeley Natl. Lab., Berkeley, Calif.
- Sweetkind, D. S., D. L. Barr, D. K. Polacsek, and L. O. Anna (1997), Integrated fracture data in support of process models, Yucca Mountain, Nevada, administrative report, *Milestone Rep. SPG32M3*, 135 pp., U.S. Geol. Surv., Denver, Colo.
- Vasco, D. W., J. E. Peterson, and E. L. Majer (1995), Beyond ray tomography: Wavepaths and Fresnel volumes, *Geophysics*, 60(6), 1790–1804.

T. M. Daley, R. Gritto (corresponding author), V. A. Korneev, E. L. Majer, and J. E. Peterson, Center for Computational Seismology, Earth Sciences Division, Lawrence Berkeley National Laboratory, MS 90-1116, 1 Cyclotron Road, Berkeley, CA 94720, USA. (tmdaley@lbl.gov; rgritto@lbl.gov; vakorneev@lbl.gov; elmajer@lbl.gov; jepeterson@lbl.gov)

M. A. Feighner, Department of Mathematics and Sciences, Solano Community College, 4000 Suisun Valley Road, Fairfield, CA 94534, USA. (mfeighne@solano.cc.ca.us)